



HAL
open science

Reappraising the production and transfer of hydrogen atoms from the middle to the upper atmosphere of Mars at times of elevated water vapor

Franck Montmessin, Denis A. Belyaev, Franck Lefèvre, Juan Alday, Margaux Vals, Anna A. Fedorova, Oleg I. Korablev, Alexander Trokhimovskiy, Michael S. Chaffin, Nicholas M. Schneider

► To cite this version:

Franck Montmessin, Denis A. Belyaev, Franck Lefèvre, Juan Alday, Margaux Vals, et al.. Reappraising the production and transfer of hydrogen atoms from the middle to the upper atmosphere of Mars at times of elevated water vapor. *Journal of Geophysical Research. Planets*, 2022, e2022JE007217 (in press). 10.1029/2022JE007217 . insu-03660797v1

HAL Id: insu-03660797

<https://insu.hal.science/insu-03660797v1>

Submitted on 6 May 2022 (v1), last revised 4 Jun 2022 (v2)

HAL is a multi-disciplinary open access archive for the deposit and dissemination of scientific research documents, whether they are published or not. The documents may come from teaching and research institutions in France or abroad, or from public or private research centers.

L'archive ouverte pluridisciplinaire **HAL**, est destinée au dépôt et à la diffusion de documents scientifiques de niveau recherche, publiés ou non, émanant des établissements d'enseignement et de recherche français ou étrangers, des laboratoires publics ou privés.

1 **Reappraising the production and transfer of hydrogen atoms from the**
 2 **middle to the upper atmosphere of Mars at times of elevated water vapor**
 3

4 **F. Montmessin¹, D. A. Belyaev², F. Lefèvre³, J. Alday^{4,6}, M. Vals¹, A. A. Fedorova², O. I.**
 5 **Korablev², A. V. Trokhimovskiy², M. S. Chaffin⁵, N. M. Schneider⁵**
 6

7 ¹LATMOS/IPSL, UVSQ Université Paris-Saclay, Sorbonne Université, CNRS, Guyancourt, France.

8 ²Space Research Institute of the Russian Academy of Sciences (IKI RAS), Moscow, Russia, Sorbonne

9 ³LATMOS/IPSL, Sorbonne Université, UVSQ Université Paris-Saclay, CNRS, Paris, France.

10 ⁴Physics Department, Oxford University, Oxford, United Kingdom.

11 ⁵Laboratory for Atmospheric and Space Physics, Boulder, Colorado, United States

12 ⁶School of Physical Sciences, The Open University, Milton Keynes, United Kingdom

13 Corresponding author. Email: franck.montmessin@latmos.ipsl.fr

14 **Key Points:**

- 15 • We decipher hydrogen production and migration to Mars' upper atmosphere using a
 16 box model for a variety of elevated water vapor cases
- 17 • H atoms formed between 60 and 80 km supply a dominant fraction of hydrogen to the
 18 upper atmosphere
- 19 • Our results suggest that perihelion climate dominates hydrogen transfer to the upper
 20 atmosphere overall

21
 22
 23
 24
 25
 26
 27
 28

29 **Abstract**

30 Water escape on Mars has recently undergone a paradigm shift with the discovery of
 31 unexpected seasonal variations in the population of hydrogen atoms in the exosphere where
 32 thermal escape occurs and results in water lost to space. This discovery led to the hypothesis
 33 that, contradicting the accepted pathway, atomic hydrogen in the exosphere was not only
 34 produced by molecular hydrogen but mostly by high altitude water vapor. Enhanced presence
 35 of water at high altitude during southern spring and summer, due to atmospheric warming and
 36 intensified transport, favors production of H through photolysis ionized chemistry of water
 37 molecules and thus appears to be the main cause of the observed seasonal variability in
 38 escaping hydrogen. This hypothesis is supported by the observation of large concentrations of
 39 water vapor between 50 km and 150 km during the southern summer solstice and global dust
 40 events. Using a simplified yet representative air parcel transport model, we show that in
 41 addition to the formation of atomic hydrogen from water photolysis above 80 km, a major
 42 fraction of the exospheric hydrogen is formed at altitudes as low as 60 km and is then directly
 43 advected to the upper atmosphere. Comparing the injection modes of a variety of events (global
 44 dust storm, perihelion periods, regional storm), we conclude that southern spring/summer
 45 controls H production and further ascent into the upper atmosphere on the long term with direct
 46 implication for water escape.

47
 48 **Plain language Summary**

49 Numerous lines of evidence suggest that Mars' water inventory was much larger in the past
 50 than it is today. The loss of this inventory has been driven by the formation of hydrated
 51 minerals on the surface, as well as by the escape of water to space. The first part of the escape
 52 process comprises the formation of H atoms, which may escape the planet once they reach
 53 the uppermost layers of the atmosphere. Here, we investigate one mechanism by which the H
 54 atoms may reach these high altitudes: the breakdown of water molecules by solar ultraviolet
 55 photons in the middle atmosphere (60-70 km above the surface), and the posterior ascent of
 56 the newly formed H atoms to the upper altitudes. We use a model that reveals that this
 57 process is the dominant contributor of atomic H to the upper atmosphere during periods of
 58 strong atmospheric circulation. In particular, we find that this mechanism is most efficient
 59 during the spring/summer season in the Southern Hemisphere, when Mars is closest to the
 60 Sun. Given that this season occurs every Martian year, our calculations suggest that this
 61 process has been the dominant contributor to water escape in the long term.

62 **1 Introduction**

63 Mars has probably lost to space a large part of its initial inventory of water and carbon
 64 dioxide (Jakosky et al., 2018) in addition to water trapped in hydrated minerals (Scheller et al.,
 65 2021). Indeed, the scars left at the surface by a previously widespread and active liquid water
 66 cycle (Carr, 1987) imply that massive amounts of water and carbon dioxide have disappeared
 67 from the planet over the ages, consequently making the presumably warm and wet primitive
 68 climate progressively transition during the last three billion years to the cold, and hyper arid
 69 climate that prevails nowadays.

70 Several studies conducted in the last decades have tried to unveil the main cause of the
 71 demise of primordial Martian water. The studies considered that a simple and still active loss
 72 mechanism is maintained indirectly by the thermal escape of hydrogen atoms in the exosphere,
 73 i.e., above an altitude of 200 km, a region where they are observed to populate the outer fringes
 74 of the atmosphere and to interact with the space environment. The theory underlying water
 75 escape has received considerable attention, as new evidence collected since 2014 have revealed
 76 major deficiencies in our initial understanding of the main mechanism controlling escape.

77 1.1 Water escape: from theory to observations

78 Water vapor is the main hydrogen carrier in the lower atmosphere of Mars. It is sourced
 79 from the massive icy deposits at the poles, which sublime in spring and summer. The
 80 conversion of water vapor in the lower atmosphere into the upper atmosphere hydrogen was
 81 initially thought to be a sluggish process paced by the formation of H₂ molecules out of H₂O
 82 dissociation (McElroy & Donahue 1972, Parkinson and Hunten, 1972). While H atoms are
 83 produced everywhere in the column, they are short lived in the lower atmosphere and cannot
 84 move away from their source region. In contrast, H₂ has a centuries long lifetime and can access
 85 the ionosphere (>100 km) where it reacts with CO₂⁺ and releases H (Krasnopolsky, 2002).

86 The key reason that explains why only H₂ is involved in this indirect hydrogen transfer
 87 to the upper atmosphere is that H₂ is not bound to condense like water is in the atmosphere. On
 88 Mars, temperature conditions make water vapor saturate at an altitude that varies with seasons
 89 and latitude, but generally lies between near the surface and the upper troposphere (above
 90 40 km). This saturation level, also referred to as the hygropause or cold trap, is supposed to cap
 91 the bulk of water vapor and confine it below. Above, water vapor sharply declines, as any water
 92 molecule exceeding vapor pressure should turn to ice. Once this vapor excess is converted into
 93 water ice cloud particles, its higher density as a solid makes it fall and release water vapor
 94 below the condensation level, sequestering water there. The initial theory for the upper H
 95 production therefore relied on the idea that, with a hygropause level being so low, water vapor
 96 alone could not be a significant carrier of H to the upper atmosphere, leaving the long-lived H₂
 97 handling most of this transfer.

98 The sequestration effect of hygropause on water vapor profile was discussed first by
 99 Davies (1979) and later evidenced by ground-based observations (Clancy et al., 1996) and the
 100 Phobos 2 mission using solar occultation in the infrared (Rodin et al., 1997). These
 101 observations led Clancy et al. (1996) to speculate about the long-term consequences of this
 102 sequestration below the hygropause. The authors argued that the colder aphelion climate should
 103 favor the retention of water in the spring/summer Hemisphere of Mars, that is, the Northern
 104 Hemisphere whose pole exposes the largest reservoir of ice.

105 Regardless of its consequences for the mobilization of the surface ice reservoir, the
 106 hygropause level has also been regarded as preventing the transfer of water to the upper
 107 atmosphere. Yet, the H₂-driven production theory has not withstood the Martian corona
 108 observations of SPICAM on Mars Express and Hubble Space Telescope that revealed
 109 unexpected changes in its brightness on a few weeks' timescale (Chaffin et al., 2014; Clarke et
 110 al., 2014). Such rapid changes are incompatible with the centuries-long steady production of
 111 H atoms imparted by H₂, which thus called for a different or additional source. The fact that
 112 enhanced coronal brightness occurred during the 2007 Global Dust Storm (GDS) led Chaffin
 113 et al. (2014) to propose that an increase in high altitude water at that time could explain the
 114 intensification of H production, and be the main contributor of water lost to space over the long
 115 term. Details on how water could become the main contributor of H were presented in Chaffin
 116 et al. (2017) who modeled the effect of water plumes deposited at a variety of altitudes from
 117 20 to 120 km and showed how fast and strong the plumes turned into an enhanced production
 118 of H atoms. The main conclusion in that study is that if sufficient water is brought up to a level
 119 where photodissociation dominates the production of H (that is above 60 km), then a rapid
 120 response is predicted for H production and escape with rates drastically changing in a timescale
 121 of weeks, therefore explaining how the Martian corona could have been observed to vary on
 122 comparable timescales. Enhanced water presence above 60 km was reported by several authors
 123 (Maltagliati et al., 2013; Fedorova et al., 2018), thereby establishing the link between enhanced
 124 high altitude water vapor and enhanced exospheric hydrogen.

125 Numerous other works have followed this study and attempted to refine these initial
 126 results (Heavens et al. 2018, Krasnopolsky, 2019; Fedorova et al. 2020; Stone et al. 2020;
 127 Fedorova et al. 2021; Chaffin et al. 2021) to address the respective contributions of isolated
 128 events (global or regional dust storms) and the global increase in dust and temperature that
 129 occurs annually around perihelion, i.e., at the transition between the southern spring and
 130 summer. Further, Krasnopolsky (2019) and Stone et al. (2020) also demonstrated that ionized
 131 chemistry can efficiently decompose high altitude water into escaping H atoms.

132 These studies provide complementary insights into the efficiency with which ionized
 133 and neutral chemistry converts high-altitude water vapor into escaping hydrogen. They endorse
 134 the idea that, on an annual basis, hydrogen thermal escape is primarily driven by the increased
 135 presence of water vapor above 60 km, which only occurs during southern spring and summer.

136 1.2 Observations of water vapor vertical distribution

137 Water vapor vertical distribution has long remained a missing product of Mars'
 138 observations. Until recently, the SPICAM infrared spectrometer onboard Mars Express has
 139 been the only asset to regularly survey water vapor vertical distribution (Fedorova et al., 2009;
 140 2018; 2021; Maltagliati et al., 2011; 2013) using solar occultation mode, a technique that
 141 provides both sensitive (between 1 and 10 parts-per-million in volume, ppmv, in H₂O volume
 142 mixing ratio, vmr) and vertically resolved (3 to 5 km vertical sampling) measurements. The
 143 enhanced presence of water vapor at high altitude during southern summer was already
 144 evidenced in some of these works, but SPICAM occultation coverage is hampered by Mars
 145 Express highly elliptical orbit, forcing an uneven temporal and latitudinal sampling, as well as
 146 by its limited detection capability.

147 With the advent of the Trace Gas Orbiter in 2018, water vapor profiles have been
 148 explored with far better accuracy and coverage through the use of state-of-the-art infrared
 149 spectrometers allowing for one to two orders better spectral resolution and sensitivity than
 150 SPICAM and taking advantage of the TGO orbit to optimize latitude/time coverage. The first
 151 surveys of water vapor accomplished by the Atmospheric Chemistry Suite (ACS) and the Nadir
 152 and Occultation for Mars Atmosphere Discovery (NOMAD) (Vandaele et al., 2019; Aoki et
 153 al., 2019; Fedorova et al., 2020) have set a new standard in profiling water, especially during
 154 southern spring and summer and also allowed for a comparison between a regular year and a
 155 year marked by a global dust storm (GDS). In particular, Belyaev et al. (2021) were able to
 156 profile, for the first time, water vapor up to 120 km using the strong water band at 2.6 μm
 157 sampled by the ACS instrument. In addition to TGO, the Neutral Gas and Ions Mass
 158 Spectrometer (NGIMS) onboard the Mars Atmosphere and Volatile Evolution (MAVEN) has
 159 sampled *in situ* the ion composition of the atmosphere above 150 km and occasionally down
 160 to 120 km during deep dips, allowing for indirect identification and quantification of water
 161 vapor in the thermosphere (Stone et al., 2020).

162 Together, TGO and MAVEN have revealed several striking features about water vapor.
 163 First, at times of dust storms which occur in the second half of the Martian year, water is
 164 observed to propagate up to >100 km and persists there for several months before disappearing
 165 by the end of the year. Not only is it observed at altitudes that were not anticipated, but it is
 166 also observed there to be in substantial quantity (i.e., 20 ppmv at 120 km, Belyaev et al., 2021),
 167 at odds with what one may expect from a hygro-pause-dominated water vapor profile. In
 168 addition, ACS, which can probe water vapor abundance and measure atmospheric temperature
 169 from the same measurement, has documented remarkably large amounts of water in excess of
 170 saturation between 60 and 80 km (saturation ratio >10, Fedorova et al., 2020), demonstrating
 171 the very high porosity of the hygro-pause and thus its reduced ability to sequester water below.

172 Finally, the dense temporal sampling of NGIMS has also shown that water transfer to the
 173 middle thermosphere (150 km) has a characteristic timescale of the order of days, with
 174 concentrations tripling in a few days (Stone et al., 2020).

175 In summary, southern summer water vapor relies on a unique combination of favorable
 176 factors (rapid transport, warm atmosphere, little to no hygropause effect) to swiftly penetrate
 177 the upper atmosphere and deliver hydrogen atoms that are subsequently released. However, the
 178 transfer of hydrogen atoms directly from their bulk source region in the middle atmosphere has
 179 never been addressed through the perspective of vertical advection that prevails during these
 180 high water events (Shaposhnikov et al., 2022) and whose nature contrasts with diffusive
 181 transport.

182 **2 Model**

183 Chaffin et al. (2017) have revealed the importance of hydrogen atom formation and
 184 transport in and from the region between 60 and 80 km, yet their model idealized the presence
 185 of water vapor at high altitudes and represented transport as a diffusive process which, by
 186 definition, ignores the unidirectional nature of advection whose strength does not depend on
 187 the tracer gradient. Such a representation of transport was also employed by Krasnopolsky
 188 (2019) who only considered the atmosphere above 80 km and specified a boundary condition
 189 for water vapor abundance at the bottom of his model. None of these studies therefore relied
 190 on a faithful representation of atmospheric transport, nor did they rely on the detailed
 191 observations of water vapor profiles that have been produced by TGO since then. These results
 192 were then analyzed using Martian GCMs, where NOMAD, ACS and MCS data were
 193 tentatively reproduced in the context of the MY34 GDS (Neary et al., 2020) or assimilated to
 194 explore the effect on escape rates of the MY34 regional C storm (Holmes et al., 2021).
 195 However, models have so far mainly focused on H atoms forming above 80 km or on particular
 196 dust storm events, leaving aside the question of the respective roles of the regular dusty
 197 perihelion climate and of isolated storms events (GDS, regional storms) in the escape budget.

198 The assumption that H production above 80 km dominates from an escape standpoint
 199 should be revisited by considering the nature of transport (advection, not diffusion) and the
 200 contribution of the atmosphere below. In that context, a different yet complementary
 201 perspective would look at the fate of a wet air parcel lifted from near the ground and
 202 progressively carried to an altitude range where H atoms are produced and then diffuse up the
 203 exobase. This supposes to adopt a Lagrangian standpoint, where one tracks over time (i.e.,
 204 altitude) the changing gaseous composition inside the parcel and can better constrain the origin
 205 of the H atoms that populate the upper atmosphere.

206 To this end, we have employed a hybrid approach combining observational results,
 207 photochemistry and transport diagnostics from a 3D Mars climate model to represent the
 208 processes affecting the composition of an air parcel over time. The rationale for this simplified
 209 approach is that the entire representation of H production, evolution, and transport cannot be
 210 based solely on observations or the 3D model. This approach of mixing observations and model
 211 results together to infer production of hydrogen in the Martian atmosphere was introduced by
 212 Alday et al. (2021) who established the prevalence of the southern spring/summer in the annual
 213 H production of the middle atmosphere.

214 Observations can only indirectly constrain the velocity of ascent in the middle
 215 atmosphere, but they can constrain directly water vapor, pressure and temperature, which are
 216 the main parameters to model the relevant photochemistry. On the other hand, given the current
 217 maturity of Mars climate models (Navarro et al., 2014; Haberle et al. 2019; Shaposhnikov et
 218 al. 2019; Neary et al., 2020; Shaposhnikov et al. 2022), using their transport diagnostics is a

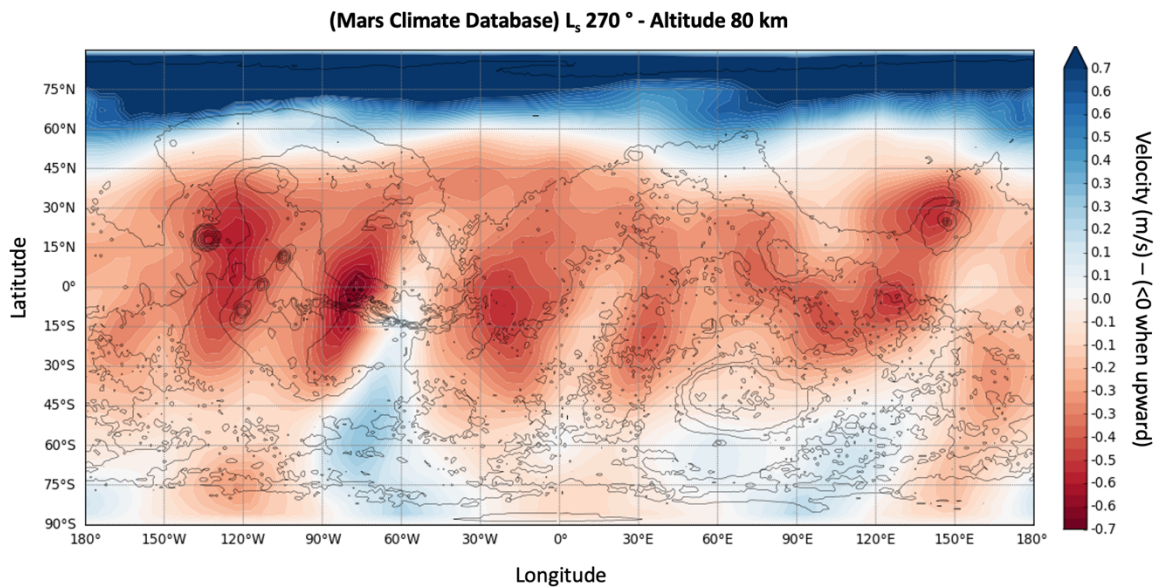
219 relevant option for specifying the range of vertical wind speeds needed for our model. An
 220 assimilation method like the one presented in Holmes et al. (2021) constitutes another way to
 221 merge observations and theory and explore the mechanisms subtending an observed
 222 atmospheric state. However, the loose coverage of TGO solar occultations (only two specific
 223 latitudes can be observed on any given day) is a strong limitation for an assimilation
 224 framework, and it is unclear how much such sparse observations can contribute to establishing
 225 an assimilated atmospheric state at very high altitude.

226 Our hybrid model tracks the fate of a wet atmospheric parcel undergoing ascent and
 227 chemistry, using the observed water vapor profiles reported in Belyaev et al. (2021) and the
 228 chemical model of Lefèvre et al. (2004) whose latest version has been presented in Lefèvre et
 229 al. (2021). We aim at tracking the variation in H number density (N_H) inside the parcel during
 230 its ascent to the upper atmosphere at times of intensified upward transport, i.e., during
 231 perihelion and during the MY34 GDS. The parcel ascends at a velocity ω of 10 cm/s as derived
 232 from the Mars Climate database (Millour et al., 2017, see Figure 1). Compared to the eddy
 233 mixing coefficient used in Chaffin et al. (2017), the upward motion predicted by the MCD is
 234 equally fast, since:

235
$$\tau_{adv} = H / \omega = 10^5 \text{ s } (\sim 1 \text{ martian day})$$

236
$$\tau_{diff} = H^2 / k_{diff} = 10^5 \text{ s}$$

237 where H is the atmospheric scale height (~ 10 km), and k_{diff} is the eddy mixing coefficient (10^7
 238 cm^2/s , see Chaffin et al., 2017 and Krasnopolsky, 2019). The typical variation of water vapor
 239 observed by NGIMS indicates that the abundance of ionized by-products of H_2O were
 240 multiplied by 2 to 3 over ~ 2 days at 150 km, supporting our assumption for ω .



241 *Figure 1: Vertical velocity as a function of longitude and latitude extracted from the*
 242 *climatological scenario of the Mars Climate Database at L_s 270°, an altitude of 80 km and*
 243 *noon time everywhere (Millour et al., 2017). Velocity is expressed in m/s (the maximum value*
 244 *is +1.7 m/s). Negative values (in red) denote upward orientation. [http://www-](http://www-mars.lmd.jussieu.fr/mcd_python/)*
 245 *mars.lmd.jussieu.fr/mcd_python/*

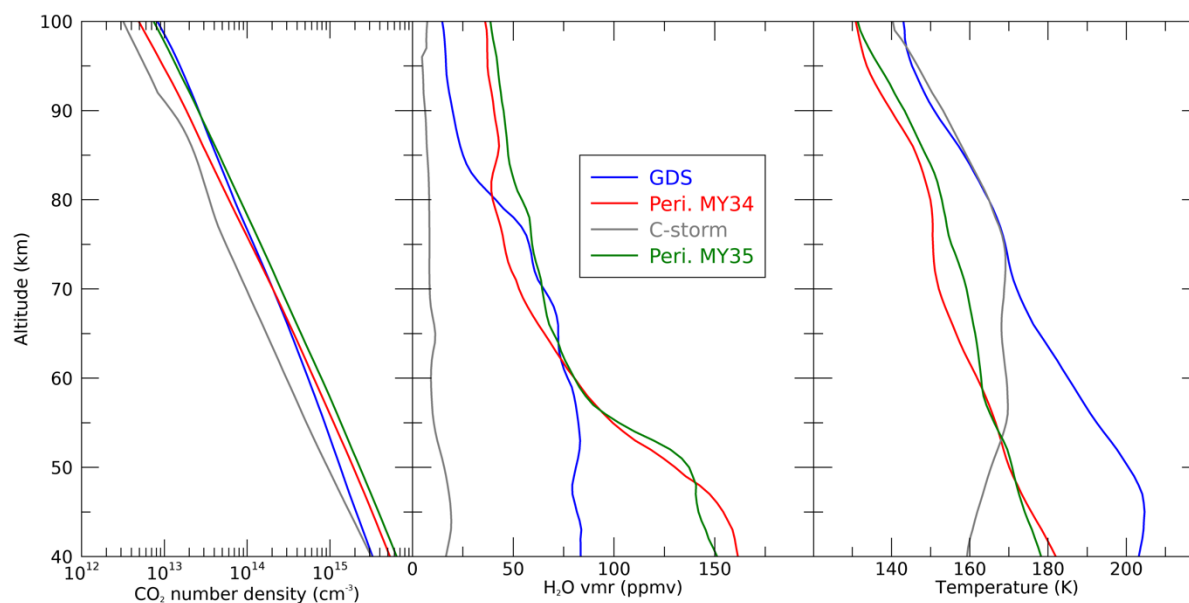
247 However, to address the sensitivity of our results to vertical speed, we also tested model
 248 response to velocities ranging from 1 to 50 cm/s as described thereafter. The vertical domain
 249 goes from the surface up to 100 km. At every time step, the concentration of water vapor inside
 250 the parcel is set to that observed by ACS at the same altitude (Belyaev et al., 2021). A net

251 budget of H atoms added/removed to/from the system is then computed by integrating H loss
 252 and production rates. H net production is only due to H₂O photolysis, while its loss is mostly
 253 due to reactions with O₃, HO₂, and O₂ (Nair., 1994). Photochemical reaction rates used in our
 254 model to determine the net production of H atoms in the parcel at every 10-meter step of its
 255 ascent were computed offline and consist of diurnal averages for the L_s considered. We did not
 256 include ionized chemistry, which is only relevant in the ionosphere (>100 km), that is located
 257 above the upper boundary of our model domain. Because the air parcel pressure decreases
 258 during its ascent, a dilution resulting from the pressure reduction induced by the parcel volume
 259 expansion between two adjacent levels is also applied to N_H.

260 3 Results

261 3.1 Periodic and stochastic events

262 One can distinguish between two modes of high-altitude water vapor migration:
 263 periodic and stochastic. The periodic mode relates to perihelion conditions as it occurs every
 264 year at the same period of time and is only driven by the reproducible evolution of the southern
 265 spring/summer climatic conditions, except when affected by the occurrence of a GDS such as
 266 in MY28. The stochastic mode corresponds to the unpredictable occurrences of dust storms,
 267 whose impact on climate is large-scale. This concerns global dust storms, and large-scale A-,
 268 B-, C- storms. Both periodic and stochastic modes occur only during the second half of the
 269 year, and it is now widely accepted that only southern spring and summer contribute to water
 270 vapor migration to the upper atmosphere (Alday et al., 2021).

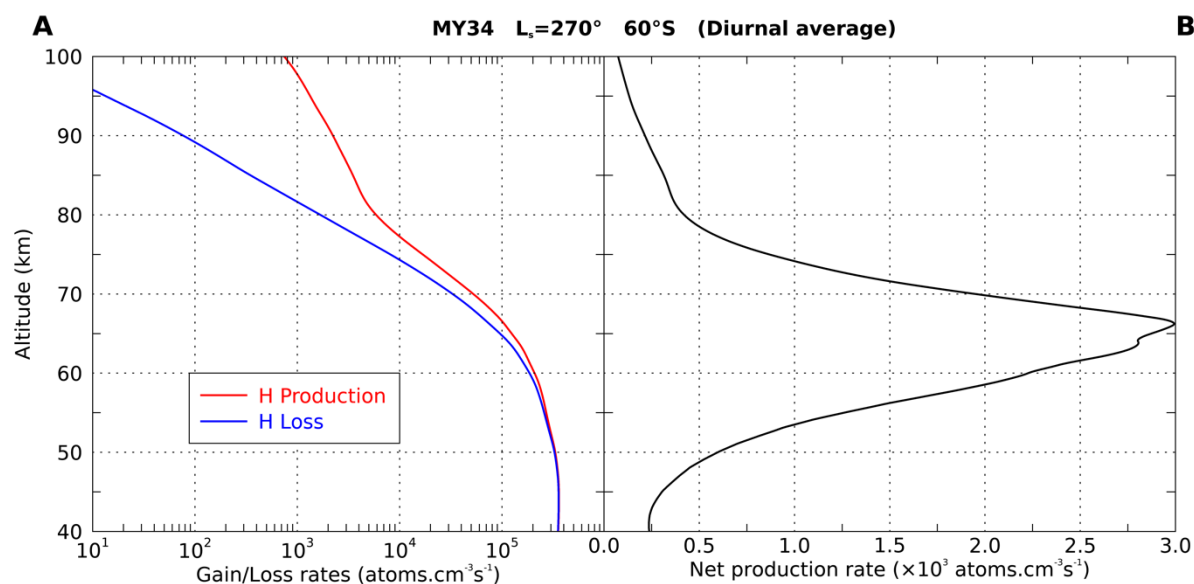


271
 272 *Figure 2: CO₂ number density, H₂O relative abundance and temperature derived from ACS*
 273 *data by Belyaev et al. (2021) for the four cases investigated in this study: MY34 GDS,*
 274 *Perihelion and C-storm, MY35 Perihelion. The smaller water abundance of the C-storm is*
 275 *potentially the result of an observational gap in ACS data.*

276 The relative importance of each mode in the long-term escape of water has been subject
 277 to debate. The main question that is addressed here is how powerful and frequent each mode
 278 of water upsurge is. All modes are characterized by sharp rises of water vapor, yet they differ
 279 in the way the atmosphere controls these rises. For instance, the MY34 GDS occurred at a time
 280 when the equinoctial circulation dominates, with a dual cell pattern centered about the equator
 281 where the rising region is thus located (Neary et al., 2020; Shaposhnikov et al., 2022). In
 282 contrast, the rise occurring around perihelion coincides with the southern solstice circulation

283 pattern, with a single cell whose rising branch is positioned in the mid-to-high southern
 284 latitudes. The strength of the southern spring/summer circulation pattern is boosted by the
 285 warmer perihelion climate and the topographic dichotomy (Richardson and Wilson, 2002).

286 Following the distinction between stochastic and periodic modes of water transfer, we
 287 selected the same periods of time as Belyaev et al. (2021) to which we added the MY34 C-
 288 storm period from the same dataset (see Figure 2). We thus based our simulations on data
 289 collected during perihelion (L_s 270°) in MY34 and MY35, as well as during the MY34 C-
 290 storm (L_s 330°), and during the climax of the MY34 GDS (195°-220°).



291
 292 *Figure 3: (A) H production and loss rates as predicted by a photochemical model for the MY34*
 293 *Perihelion case, using pressure, temperature, and water vapor profiles obtained by ACS MIR*
 294 *channel. H production is only due to water vapor photolysis. H loss relies on reactions with*
 295 *O₃, HO₂, and O₂. (B) H net budget calculated by subtracting loss from production rates.*

296 For simplicity, we assume that each simulation is representative of the transport and
 297 thermodynamical conditions encountered by water for each period of interest. Therefore, we
 298 conducted four simulations. Results were obtained for a particular latitude range that
 299 theoretically corresponds to the main zone of H ascent (i.e., 60°S for Perihelion and C-Storm,
 300 0° for the GDS).

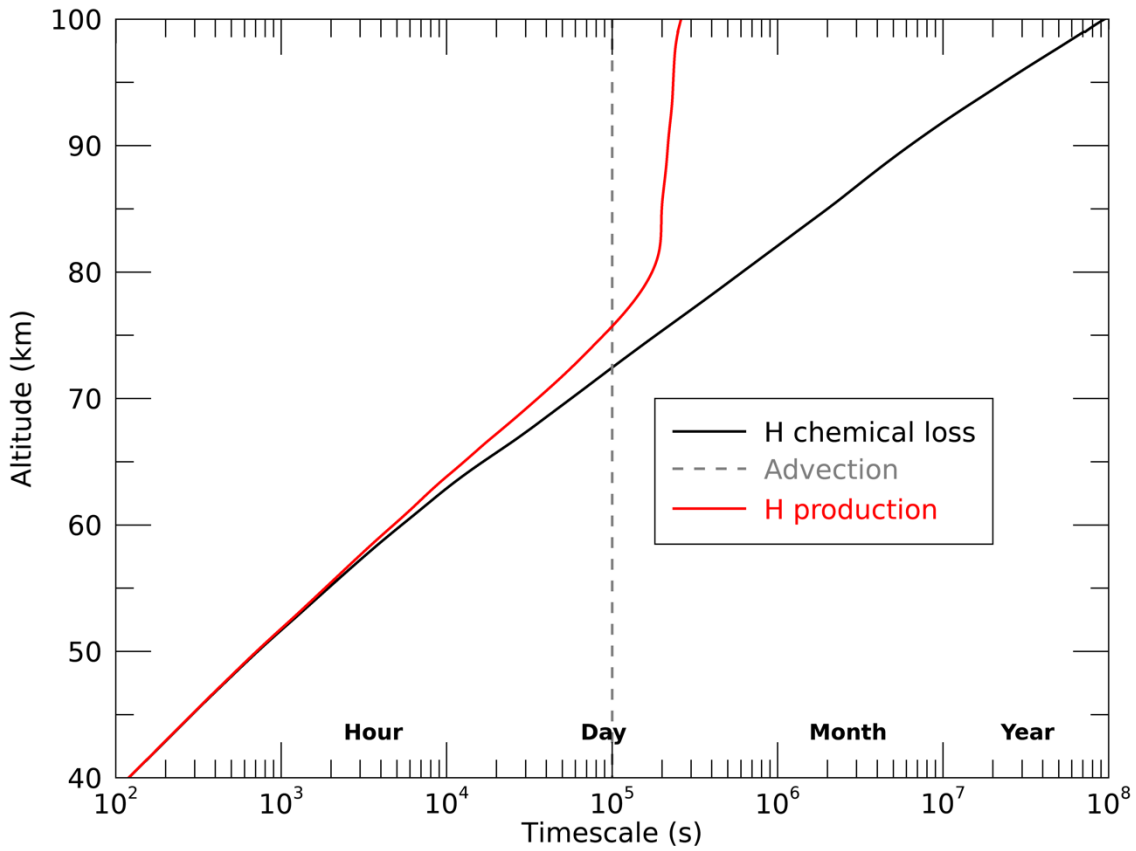
301 3.2 MY34 Perihelion

302 Here we consider the particular situation occurring during the transition between
 303 southern spring and summer and that is henceforth referred to as the Perihelion season and that
 304 encompasses the period from L_s 240° to 270°. Alday et al. (2021) demonstrated the prevalence
 305 of the Perihelion season for the formation of H and D atoms at 60 km of altitude. This
 306 conclusion was based on applying theoretical photolysis rates upon HDO and H₂O profiles
 307 observed by ACS.

308 3.2.1 Timescale Consideration

309 Figure 3-A shows that H chemical loss balances photolysis production up to ~50 km,
 310 above which production dominates loss increasingly with altitude. Therefore, H atoms can only
 311 ascend if they are produced above 50 km. The net production rate (Figure 3-B) peaks at ~65 km
 312 since, at the same time, the number density of water vapor from which H is directly produced
 313 declines with pressure. H atoms produced below 60 km do not contribute to the transfer of H

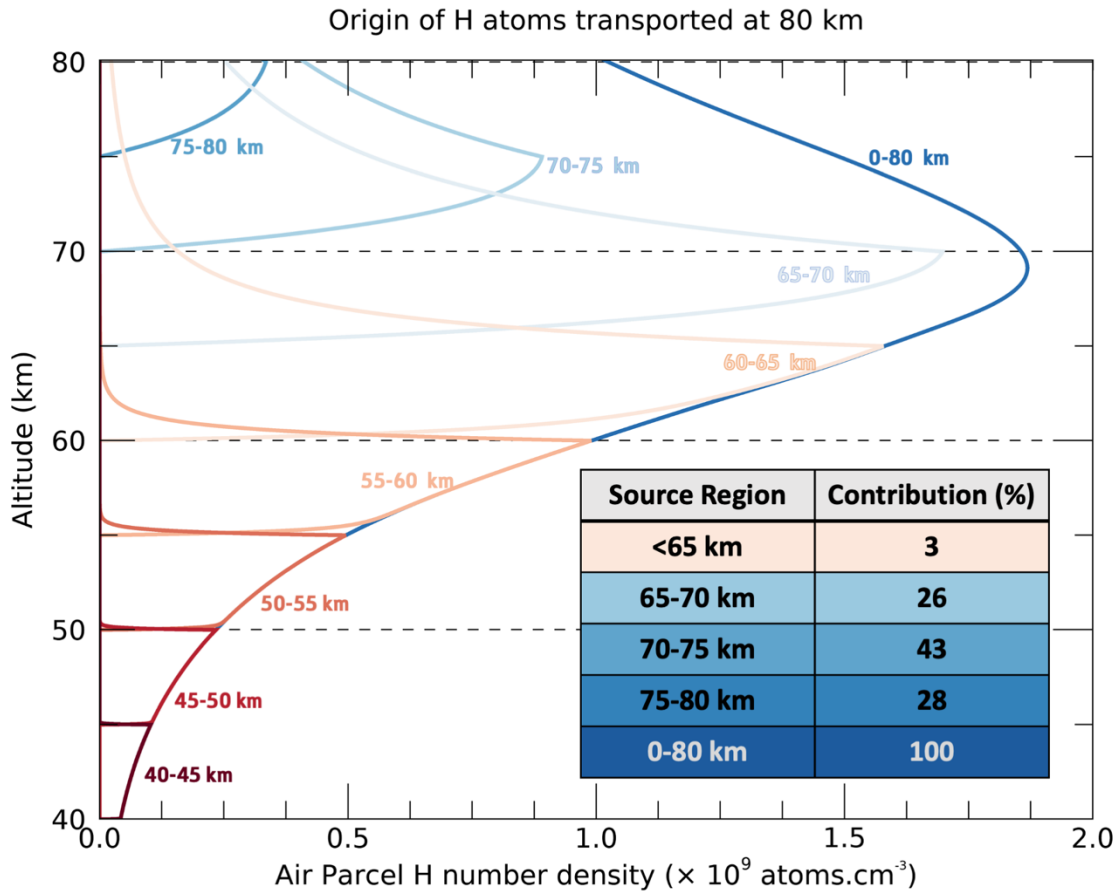
314 to the upper atmosphere above 80 km, since loss operates >10 times faster than advection
 315 (hours vs. days, see Figure 4), as explained in Section 3.4.



316 *Figure 4: Timescales associated with the various processes represented in the air parcel*
 317 *model, transport timescale is deduced from an ascent*
 318 *velocity of 10 cm/s.*
 319

320 3.2.2 Hydrogen origin in the lower atmosphere

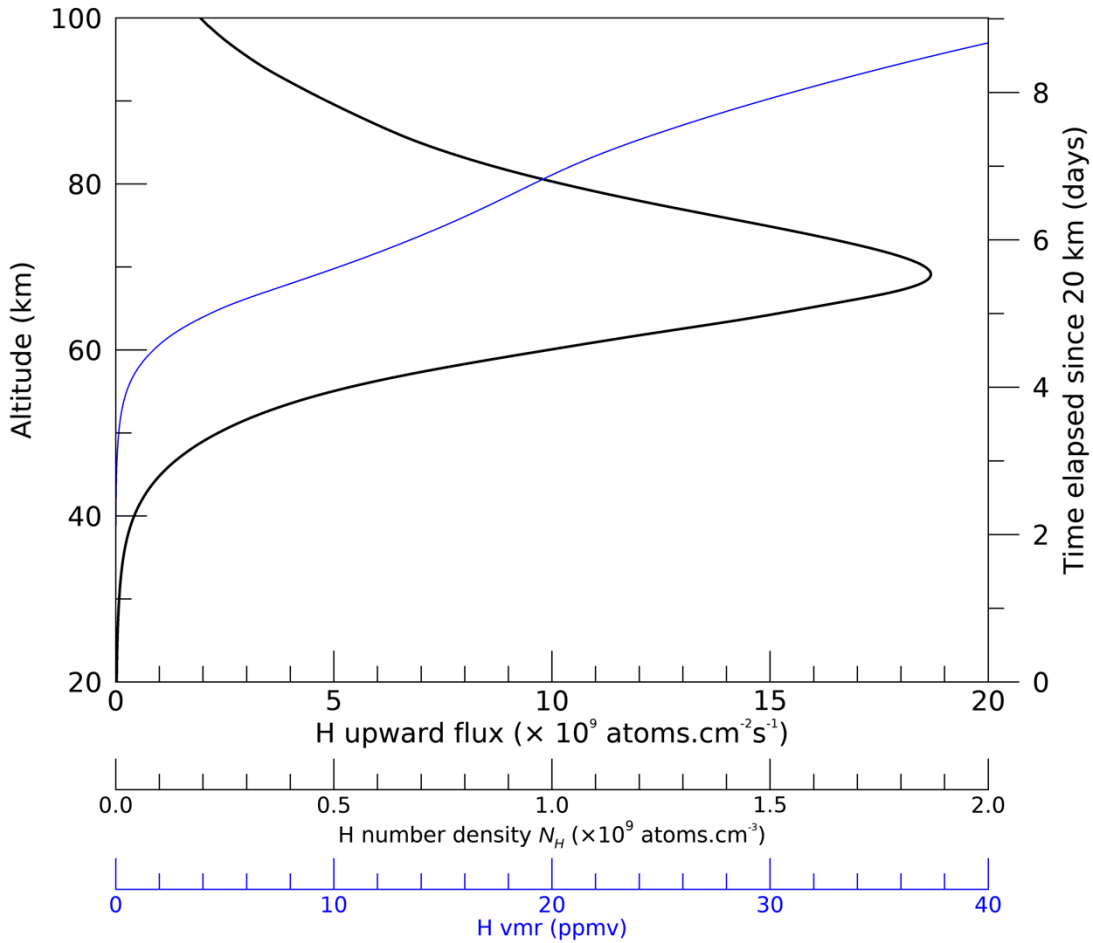
321 Our air parcel model can be used to track the origin of the H atoms advected to 80 km
 322 (Figure 5). To do so, we restrict production inside 5-km atmospheric layers located between
 323 40 and 80 km (Figure 5). Our model confirms that no H atoms produced below 60 km can
 324 access the upper atmosphere as it is bound to recombine before reaching 80 km, which implies
 325 that almost no atoms produced in the peak production region contribute to escape. After being
 326 advected from their production zone below 60 km, H atoms are completely lost after 1 or 2 km
 327 of ascent. The production zone that matters for escape comprises altitudes from 65 to 80 km,
 328 with a dominant contribution from the 70 to 75 km region.



329
 330 *Figure 5: Air parcel model predictions for a set of configurations where production only occurs*
 331 *in a 5 km-thick layer whose top altitude we vary from 45 to 80 km. Plotted quantity is the H*
 332 *number density (atoms.cm⁻³) in the parcel. The shape of each curve reflects the processes at*
 333 *work inside the parcel during its ascent at 10 cm/s. Below 55 km, H is instantaneously lost*
 334 *after leaving its production zone. Then, its increasing lifetime allows it to ascend several km*
 335 *before destruction. Above 60 km, an increasing fraction of the produced atoms can be advected*
 336 *up to 80 km. The contribution of each 5 km layer is calculated by dividing their corresponding*
 337 *N_H at 80 km with that of the 0-80 km case, that is the nominal full production case.*

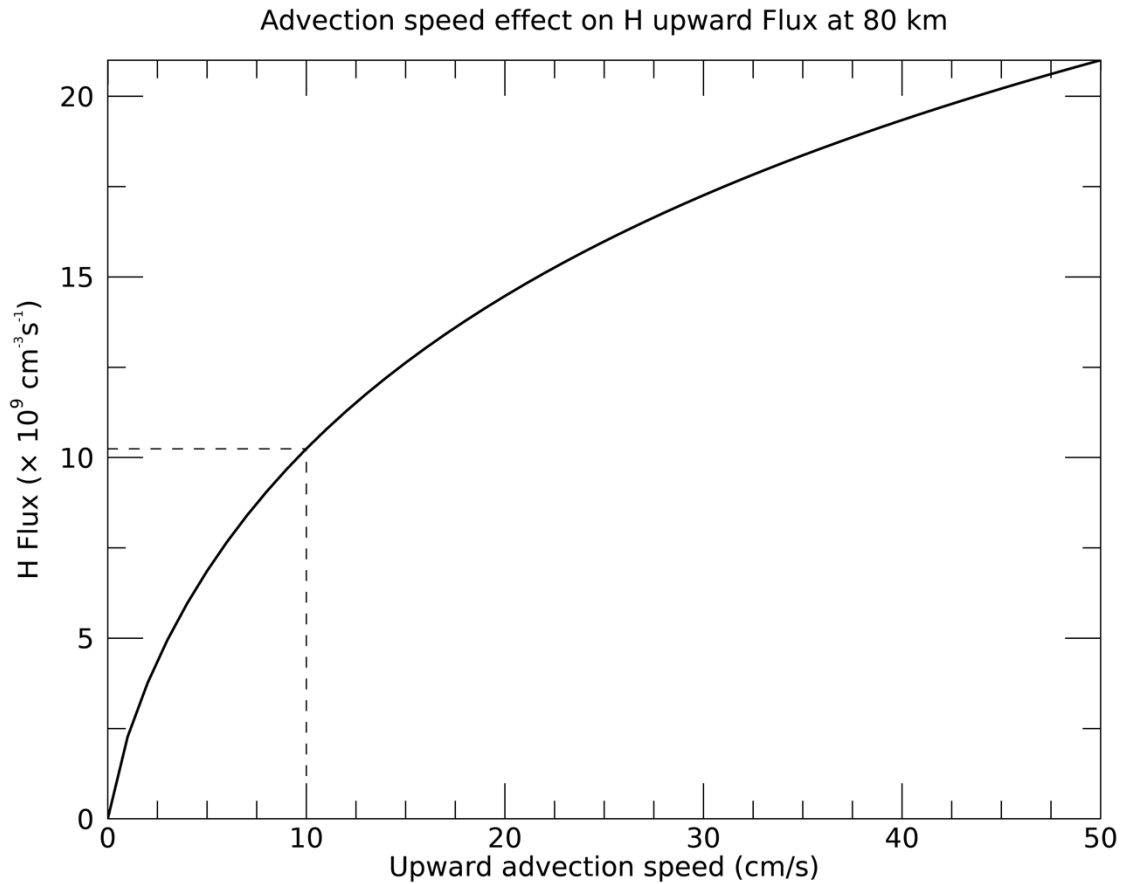
338 **3.2.3 Upward Flux**

339 Figure 6 shows the altitude (or equivalently time, on the right axis) evolution of the
 340 hydrogen number density (N_H) in the air parcel and the corresponding upward flux (equal to
 341 $N_H \times \omega$). N_H shows a pronounced peak of 1.9×10^9 atoms.cm⁻³ at 69 km that is reminiscent of
 342 the net production peak found at 65 km. However, as explained earlier, N_H then decreases after
 343 rising above the peak as subsequent H production diminishes and cannot compensate dilution
 344 subsequent to the parcel volume expansion.



345
 346 *Figure 6: Model results for the H number density in the parcel (N_H) and the resulting upward*
 347 *flux for the MY34 perihelion case (black solid line). Contrasting with the N_H profile and its*
 348 *pronounced peak at 70 km, the H volume mixing ratio (vmr) profile (blue line) exhibits a*
 349 *constant increase from 55 km up to 100 km. Note that the $1.1 \times 10^{10} \text{ cm}^{-2}\text{s}^{-1}$ flux value found at*
 350 *80 km is nearly 50 times greater than the canonical escape rate of $\sim 2 \times 10^8 \text{ cm}^{-2}\text{s}^{-1}$ deduced*
 351 *from H_2 dominated formation of upper atmospheric H (Krasnopolsky, 2019; Stone et al., 2020).*

352 At 80 km, we find that the upward hydrogen flux is of $1.1 \times 10^{10} \text{ cm}^{-2}\text{s}^{-1}$, a value that is
 353 nearly twice the net photolysis product of H integrated from 80 to 100 km. The H flux at the
 354 bottom of the upper atmospheric domain is not only significant, it actually accounts for a
 355 dominant portion of the H budget in the upper atmosphere of the southern summer, when H is
 356 known to escape massively.



357
 358 *Figure 7: Sensitivity of the simulated H flux at 80 km to upward velocity in the case of the*
 359 *MY34 Perihelion simulation. Our baseline has a velocity of 10 cm/s, yet even a twofold increase*
 360 *or decrease in velocity only impacts H flux by ~40%.*

361 **3.2.4 Sensitivity to ascent speed**

362 At an upward speed of 10 cm/s, it takes roughly a day for the parcel to ascend 10 km in
 363 altitude. The derived H flux at a given altitude being the product of ascent speed with the H
 364 number density in the parcel, a change in speed linearly affects this product. However, it also
 365 indirectly affects it through the H number density in the parcel. Indeed, N_H is history-
 366 dependent, as it integrates over time the effects of local conditions on loss and production in
 367 the parcel. In turn, the effect of local conditions on H budget depends on the residence time of
 368 the parcel at a given altitude, and thus on its ascent speed. Therefore, a higher ascent speed also
 369 implies the parcel spends less time in regions where it can accumulate H atoms.

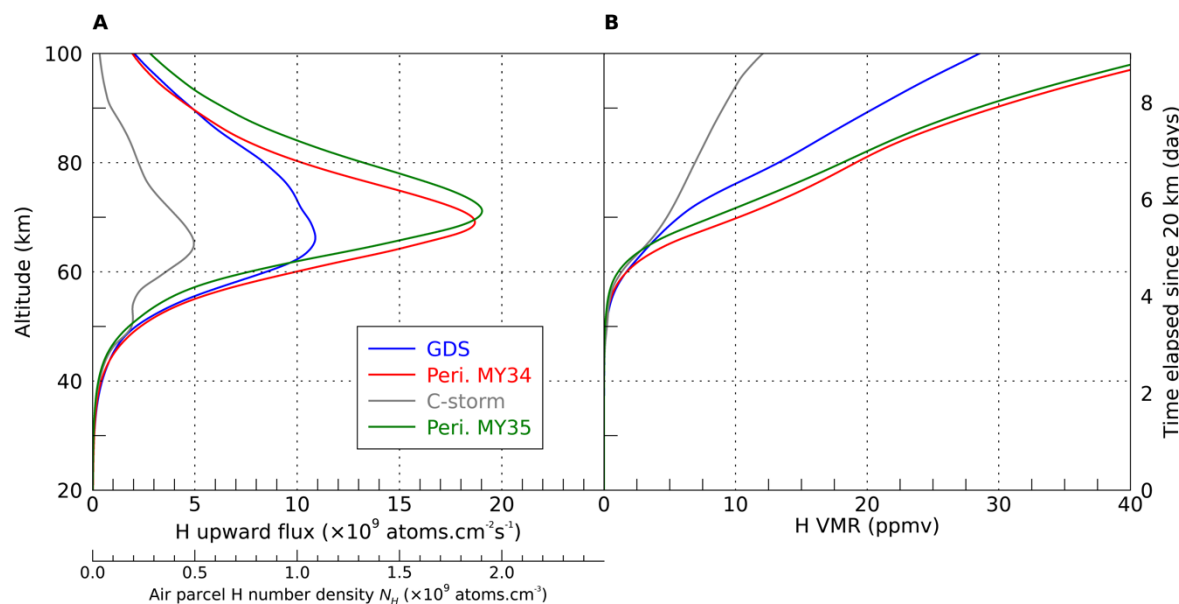
370 This antagonism of effects explains the parabolic shape of the H flux dependence to
 371 ascent speed, as displayed in Figure 7, and additionally give our results on the 80 km H flux
 372 some immunity to speed uncertainty.

373 **3.3 Other cases**

374 **3.3.1 Result Comparison**

375 The MY34 configuration described above has revealed the main characteristics of the
 376 H migration phenomenon, showing the significance of the H flux at 80 km and the partitioning
 377 of the H origin among the atmospheric layers located below and in particular between 60 and

378 80 km. We then subsequently applied our model to the three other configurations of interest:
 379 MY35 Perihelion, MY34 GDS and MY34 C-storm (see Figures 2 and 8). It is to be noted that
 380 a large part of the C-storm was not monitored by ACS due to TGO's orbit constraints. The data
 381 gap actually covers the peak activity of this regional storm, which implies our results
 382 underestimate the C-storm upward flux, since its water vapor profile exhibits distinctly smaller
 383 abundances compared to other cases (Figure 2). Yet, this event produced an intense brightening
 384 of the hydrogen corona (Chaffin et al., 2021).



385
 386 *Figure 8: A synthesis of the four configurations explored with the air parcel model: GDS,*
 387 *MY34 and MY35 Perihelion, MY34 C-storm. (A) H Upward flux and concentration in the*
 388 *parcel during its rise from 20 to 100 km. (B) Same as (A) except N_H is converted into H vmr*
 389 *(ppmv).*

390 MY34 and MY35 Perihelion cases are in remarkable agreement, both exhibiting the
 391 same upward flux profile (Figure 8) with a pronounced peak around 70 km only slightly shifted
 392 upward in MY35. This altitude offset explains why the MY35 80 km H flux is ~30% larger
 393 than MY34, as a higher proportion of H atoms are produced closer to the 80 km boundary.
 394 Indeed, water vapor is 15 ppmv more abundant in MY35 at 80 km, which then directly impacts
 395 H production and upward flux (Figure 2). These results support the idea that the perihelion
 396 configuration is highly reproducible from year to year, which provides confidence for
 397 extrapolating its contribution in the escape budget on a longer term.

398 The GDS case exhibits a H flux profile that is significantly flared compared to the
 399 perihelion case, reflecting the distinct H₂O vmr profile of the GDS that shows a nearly uniform
 400 mixing ratio of ~70 ppmv below 70 km. The GDS H flux has a maximum value located at 65
 401 km that is twice smaller than for perihelion cases. At 80 km, GDS flux remains distinctly
 402 smaller than the two perihelion seasons considered here. However, at 85 km, the GDS flux
 403 catches up with MY34 Perihelion flux. The broadened peak of the GDS implies that a larger
 404 proportion (~50%) of the H population origin is located close to the 80 km boundary. In
 405 addition, the total density of the MY34 GDS above 80 km is higher than for perihelion cases
 406 (Figure 2), which mitigates the volume expansion (dilution) effect on the air parcel in this
 407 altitude range.

408 3.3.2 Upward flux vs. neutral photolysis above 80 km

409 Considering that other processes are at work above 80 km, it is interesting to determine
 410 how the upward H flux at 80 km compares, in terms of hydrogen input into the region above
 411 80 km, with these other processes. One of them is the direct deposition of hydrogen from water
 412 photolysis above 80 km. We mentioned earlier that in the case of MY34 perihelion, the upward
 413 flux was about twice the net column production of H atoms out of photolysis between 80 and
 414 100 km. We expanded this comparison to all other cases and found the following: (i) for MY35
 415 perihelion, the upward flux was 55% greater than local photolysis production, (ii) for the MY34
 416 GDS, the upward flux was 30% greater, and (iii) for the MY34 C-storm, the upward flux was
 417 nearly three times higher than local production.

418 These results imply that the upward influx of H at the bottom of the upper atmospheric
 419 domain is the dominant supplier in the context of the neutral photochemistry.

420 3.3.3 Upward flux vs. ionized chemistry

421 Without water at high altitude, H is only produced out of the reaction between CO_2^+
 422 and H_2 , leading to a column production rate of the order of $1.6 \times 10^8 \text{ cm}^{-2}\text{s}^{-1}$ (Krasnopolsky,
 423 2019). This H_2 chemical path supplies a background of H atoms all year long that is
 424 independent of the quantity of water vapor in the upper atmosphere.

425 However, Krasnopolsky (2019) completed the H_2 pathway with ionized chemistry
 426 involving water and triggered by H_2O reacting with CO_2^+ . He estimated that water chemistry
 427 in the thermosphere was producing H at a rate equal to:

428
$$\phi_{\text{H}\uparrow} (\text{cm}^{-2}\text{s}^{-1}) = 1.6 \times 10^8 + 1.4 \times 10^7 f_{\text{H}_2\text{O}}^*(\text{ppm})$$

429 which, in the case water has 60 ppmv relative abundance at 80 km, yields an H escape rate of
 430 $10^9 \text{ cm}^{-2}\text{s}^{-1}$.

431 Stone et al. (2020) describe a series of high altitude (150 km) NGIMS in situ
 432 measurements of ionized water by-products that they used as a proxy to estimate water vapor
 433 local concentration. They then applied an ionized chemistry model similar to Krasnopolsky
 434 (2019) to infer the production of H atoms out of H_2O reactions with CO_2^+ . These authors found
 435 a net production rate of $2.8 \times 10^9 \text{ cm}^{-2}\text{s}^{-1}$.

436 The difference of results between these two studies is not easily tractable, yet may be
 437 explained by the fact that Stone et al. (2020) directly constrained their model with NGIMS
 438 measurements that probed the ion composition of the atmosphere down to ~ 125 km during a
 439 MAVEN deep dip, and possibly because they employed updated reaction rates compared to
 440 Krasnopolsky (2019). Yet, both rely on the same approach and concur on the fact that ionized
 441 chemistry of water dominates over H_2 chemistry and is a major supplier of escaping H atoms
 442 at times of “high water”. Stone et al. (2020) further advocated that MY34 GDS produced such
 443 a change in the ion by-products of water that GDS are likely to represent the main escape
 444 process for water overall.

445 3.3.4 Implication for escape

446 Assuming that the H atoms crossing the 80 km boundary can be then carried up to
 447 escape altitudes, our results shed light on the potential of each event for hydrogen escape.
 448 Table 1 summarizes the production rates computed for most of the events discussed here and
 449 for the various H production modes that have been studied so far. Of all the processes involved
 450 in the production and injection of H atoms into the upper atmosphere, the upward transfer is
 451 found to be systematically greater than production from water photolysis or ionized chemistry.

452 This statement is only valid outside the cold aphelion period, where H₂ molecules are the main
 453 precursor of H atoms.

H production type in column rate (atoms per cm ⁻² s ⁻¹)		Event type		
		Perihelion MY34 / MY35	Global Dust Storm	C-storm
H ₂ -CO ₂ ⁺ chemistry		1.6 × 10 ⁸ (k19)	1.6 × 10 ⁸ (k19)	1.6 × 10 ⁸ (k19)
H ₂ O-CO ₂ ⁺ chemistry		1 × 10 ⁹ (k19)	2.38 × 10 ⁹ (s20)	
This study	H ₂ O photolysis (80-100 km)	5 × 10 ⁹ / 7.5 × 10 ⁹	5.4 × 10 ⁹	7 × 10 ⁸
	H upward flux	1 × 10 ¹⁰ / 1.3 × 10 ¹⁰	8.4 × 10 ⁹	2.2 × 10 ⁹

454 *Table 1: a synthesis of the results obtained in this study and compared with other works (k19:*
 455 *Krasnopolsky, 2019; s20: Stone et al., 2020).*

456 This raises the question of the fate of H atoms crossing the 80 km boundary.
 457 Shaposhnikov et al. (2022) explore the dynamical mechanisms that carry volatiles into the
 458 upper atmosphere at GDS and perihelion times. Using a Mars' GCM to address the gravity
 459 wave breaking effect on global circulation and the transport of water at high altitude, they show
 460 that atmospheric updrafts are the main carrier of volatiles up to 100 km, above which molecular
 461 diffusion combines with advection and then controls above 120 km the ascent of gases to the
 462 exobase. It is therefore legitimate to apply our advective transport model to hydrogen atoms
 463 produced below 80 km. Since the lifetime of hydrogen atoms increases steadily with altitude,
 464 once they have entered the upper atmospheric domain above 80 km, they are likely to reside
 465 there long enough for a significant fraction of them to reach the exobase. In fact, the way
 466 circulation is organized at times of high water events implies a massive upwelling either at the
 467 equator (GDS) or at high southern latitudes (perihelion) compensated by a massive
 468 downwelling at the pole(s). Figure 1 gives a good illustration of the upwelling and downwelling
 469 effects on the vertical velocity field. During perihelion, downwelling velocity is twice larger
 470 than upwelling (1.7, not shown, vs. 0.7 m/s maximum values) yet is confined into a narrow
 471 band at the north pole. Our air parcel concept only captures the ascent part of the hydrogen
 472 journey into the upper atmosphere. At 100 km, that is at the top of our model, molecular
 473 diffusion will then take over the rest of the ascent that will lead released H atoms to escaping
 474 altitude. Yet a fraction of these atoms will eventually return to the middle atmosphere via the
 475 downwelling region.

476 Depending on the value of this fraction, our model for direct H injection into the upper
 477 atmosphere consequently appears as a plausible dominant contributor to H escape overall. At
 478 least, the upward transport of H atoms is comparable in strength with the direct deposition of
 479 H atoms from water photolysis above 80 km. This consideration is in line with the Chaffin
 480 mechanism, except our study allows disentangling the role and contribution of its principal
 481 components, namely transport from the middle atmosphere and production by photolysis.

482 3.3.5 Perihelion: the preferred period for H escape?

483 Our comparison found a very consistent behavior of the H flux around perihelion for
 484 two consecutive years. It is premature to conclude on the role of the GDS on the long-term
 485 escape of water, considering that the MY34 GDS was a particular type of GDS (yet replicating

486 the time period of the MY25 GDS) which have been observed at other times in the Southern
487 spring and summer (the MY28 GDS started at L_s 270°). However, within the framework and
488 constraints of this study, we find that the perihelion period supplies on any given year at least
489 as much as the GDS did in MY34. Considering that GDS have been observed to occur every
490 >3 Martian years, on the long term (that is within the shortest of the orbital cycle), perihelion
491 likely remains the dominant season for conveying H atoms in the upper atmosphere, thereby
492 imprinting a dominant effect on escape. On top of it, regional storms shall add to this hydrogen
493 transfer. Their relative importance is more difficult to evaluate, as only a fraction of a single
494 event (the 2018 C-storm) could be tested with our model, which delivered results arguably
495 underestimating the H flux.

496 There are however reasons to argue that perihelion climate controls the transfer of H
497 overall. First, the warmer and dustier conditions of the perihelion climate last $\sim 60^\circ L_s$, a
498 duration comparable to GDS' and which is greater than the duration of regional storms. Second,
499 perihelion corresponds to the seasonal maximum in the strength of the global Hadley
500 circulation, which is additionally boosted by the topographic dichotomy. Third, the higher solar
501 input of perihelion implies that a smaller amount of dust is needed to produce the same
502 warming as extra-perihelion events. In contrast, the effect of regional storms on H upward flux
503 relies on how much dust regional storms do lift, which is variable from year to year as shown
504 in the climatology of dust column opacity (see Figure 16 in Montabone et al., 2015).

505 4 Conclusion

506 We have used a 1D hybrid model to represent the ascent of a wet air parcel at times of
507 intense dust and transport activity. This model combines observations of the ACS instrument
508 onboard TGO that measured, for the first time, water vapor abundance from 20 to 120 km
509 (Belyaev et al., 2021). These observations enable the in-depth study of how the water vapor
510 penetration to high altitude contributes to hydrogen production above 80 km. In contrast with
511 other 1D models that have been used to explore Mars' photochemistry, our model does not
512 represent the vertical transport through the standard eddy diffusion but through advection with
513 a constant velocity of 10 cm/s up to 100 km. This choice more faithfully represents the way air
514 masses are elevated during periods of high water events and intensified circulation.

515 We then combined the air parcel advection with ACS water vapor measurements and a
516 detailed model of the neutral photochemistry to track the H concentration (or number density)
517 in the parcel during its ascent. We find the production and further advection of H atoms from
518 60 to 80 km supply an upward flux of hydrogen that overwhelms all other modes of hydrogen
519 production in the upper atmosphere. The upward flux shows a slight dependence on the ascent
520 velocity, which thus mitigates the importance of specifying the correct velocity when
521 comparing different events together.

522 Our results imply that, contrary to a common assumption made in models used to study
523 Mars' photochemistry and escape processes, the region between 60 and 80 km cannot be
524 neglected in the production and migration of hydrogen to the upper atmosphere. In particular,
525 these results imply that upper atmosphere photochemistry models intending to capture
526 Southern Summer conditions need to carefully consider the flux boundary condition for H at
527 the lower boundary if it is higher than 80 km.

528 Testing a variety of configurations, from the MY34 GDS to the recent MY35 perihelion
529 period, we have been able to assess how the hydrogen upward flux from above 60 km varies
530 with events. Stochastic events (GDS and A, B, C- storms) have a strong imprint on the escape
531 budget, but our results suggest perihelion remains the dominant escape component on the long
532 term.

533 **Acknowledgements**

534 ExoMars is the space mission of ESA and Roscosmos. The ACS investigation was developed
 535 by the Space Research Institute (IKI) in Moscow, and the Laboratoire Atmospheres, Milieux,
 536 Observations Spatiales (LATMOS) in Guyancourt. The investigation was funded by
 537 Roscosmos, the National Centre for Space Studies of France (CNES) and RSF (Russian
 538 Science Foundation 20-42-0903). This work was funded by CNES, the Agence Nationale de
 539 la Recherche (ANR, PRCI, CE31 AAPG2019, MCUBE project), DIM ACAV labelled by the
 540 Ile-de-France region in support for the research (Domaine d'Intérêt Majeur, Astrophysique et
 541 Conditions d'Apparition de la Vie)".

542 **Data availability**

543 The ACS data used in this study are published in Belyaev et al. (2021) and can be found at
 544 [https://data.mendeley.com/datasets/995y7ymdgm/draft?a=daa72362-898d-4c86-8a13-](https://data.mendeley.com/datasets/995y7ymdgm/draft?a=daa72362-898d-4c86-8a13-023b4b59134c)
 545 [023b4b59134c](https://data.mendeley.com/datasets/995y7ymdgm/draft?a=daa72362-898d-4c86-8a13-023b4b59134c).

546 The data produced by our model can be obtained (for review purpose) on the following link:
 547 <https://mycore.core-cloud.net/index.php/s/na60fDZRoNCGa6i>

548 These data will be deposited after the review on the ESPRI/IPSL archive server, at which
 549 point a doi will be created.

550 **References**

- 551 Alday, J., Trokhimovskiy, A., Irwin, P. G. J., Wilson, C. F., Montmessin, F., Lefèvre, F., et
 552 al. (2021). Isotopic fractionation of water and its photolytic products in the atmosphere
 553 of Mars. *Nature Astronomy*. <https://doi.org/10.1038/s41550-021-01389-x>
- 554 Aoki, S., Vandaele, A. C., Daerden, F., Villanueva, G. L., Liuzzi, G., Thomas, I. R., et al.
 555 (2019). Water Vapor Vertical Profiles on Mars in Dust Storms Observed by
 556 TGO/NOMAD. *Journal of Geophysical Research: Planets*, *124*(12), 3482–3497.
 557 <https://doi.org/10.1029/2019JE006109>
- 558 Belyaev, D. A., Fedorova, A. A., Trokhimovskiy, A., Alday, J., Montmessin, F., Korablev,
 559 O. I., et al. (2021). Revealing a High Water Abundance in the Upper Mesosphere of
 560 Mars With ACS Onboard TGO. *Geophysical Research Letters*, *48*(10).
 561 <https://doi.org/10.1029/2021GL093411>
- 562 Carr, M. H. (1987). Water on Mars, *326*, 30–35. <https://doi.org/10.1038/326030a0>
- 563 Chaffin, Michael S., Chaufray, J.-Y., Stewart, I., Montmessin, F., Schneider, N. M., &
 564 Bertaux, J.-L. (2014). Unexpected variability of Martian hydrogen escape: *Geophysical*
 565 *Research Letters*, *41*(2), 314–320. <https://doi.org/10.1002/2013GL058578>
- 566 Chaffin, M. S., Deighan, J., Schneider, N. M., & Stewart, A. I. F. (2017). Elevated
 567 atmospheric escape of atomic hydrogen from Mars induced by high-altitude water.
 568 *Nature Geoscience*, *10*(3), 174–178. <https://doi.org/10.1038/ngeo2887>
- 569 Chaffin, M. S., Kass, D. M., Aoki, S., Fedorova, A. A., Deighan, J., Connour, K., et al.
 570 (2021). Martian water loss to space enhanced by regional dust storms. *Nature*
 571 *Astronomy*, *5*(10), 1036–1042. <https://doi.org/10.1038/s41550-021-01425-w>
- 572 Clancy, R. T., Grossman, A. W., Wolff, M. J., James, P. B., Rudy, D. J., Billawala, Y. N., et
 573 al. (1996). Water vapor saturation at low latitudes around aphelion: A key to Mars
 574 climate? *Icarus*, *122*, 36–62.

- 575 Clarke, J. T., Bertaux, J.-L., Chaufray, J.-Y., Gladstone, G. R., Quemerais, E., Wilson, J. K.,
 576 & Bhattacharyya, D. (2014). A rapid decrease of the hydrogen corona of Mars: the
 577 Martian Hydrogen Corona. *Geophysical Research Letters*, 41(22), 8013–8020.
 578 <https://doi.org/10.1002/2014GL061803>
- 579 Davies, D. W. (1979). The vertical distribution of Mars water vapor. *Journal of Geophysical*
 580 *Research*, 84(B6), 2875. <https://doi.org/10.1029/JB084iB06p02875>
- 581 Fedorova, A. A., Korablev, O. I., Bertaux, J.-L., Rodin, A. V., Montmessin, F., Belyaev, D.
 582 A., & Reberac, A. (2009). Solar infrared occultation observations by SPICAM
 583 experiment on Mars-Express: Simultaneous measurements of the vertical distributions
 584 of H₂O, CO₂ and aerosol. *Icarus*, 200(1), 96–117.
 585 <https://doi.org/10.1016/j.icarus.2008.11.006>
- 586 Fedorova, A., Bertaux, J.-L., Betsis, D., Montmessin, F., Korablev, O., Maltagliati, L., &
 587 Clarke, J. (2018). Water vapor in the middle atmosphere of Mars during the 2007 global
 588 dust storm. *Icarus*, 300, 440–457. <https://doi.org/10.1016/j.icarus.2017.09.025>
- 589 Fedorova, A. A., Montmessin, F., Korablev, O., Luginin, M., Trokhimovskiy, A., Belyaev,
 590 D. A., et al. (2020). Stormy water on Mars: The distribution and saturation of
 591 atmospheric water during the dusty season. *Science*, 367(6475), 297–300.
 592 <https://doi.org/10.1126/science.aay9522>
- 593 Fedorova, A., Montmessin, F., Korablev, O., Lefèvre, F., Trokhimovskiy, A., & Bertaux, J.
 594 (2021). Multi-Annual Monitoring of the Water Vapor Vertical Distribution on Mars by
 595 SPICAM on Mars Express. *Journal of Geophysical Research: Planets*, 126(1).
 596 <https://doi.org/10.1029/2020JE006616>
- 597 Haberle, R. M., Kahre, M. A., Hollingsworth, J. L., Montmessin, F., Wilson, R. J., Urata, R.
 598 A., et al. (2019). Documentation of the NASA/Ames Legacy Mars Global Climate
 599 Model: Simulations of the present seasonal water cycle. *Icarus*, 333, 130–164.
 600 <https://doi.org/10.1016/j.icarus.2019.03.026>
- 601 Heavens, N. G., Kleinböhl, A., Chaffin, M. S., Halekas, J. S., Kass, D. M., Hayne, P. O., et
 602 al. (2018). Hydrogen escape from Mars enhanced by deep convection in dust storms.
 603 *Nature Astronomy*, 2(2), 126–132. <https://doi.org/10.1038/s41550-017-0353-4>
- 604 Holmes, J. A., Lewis, S. R., Patel, M. R., Chaffin, M. S., Cangi, E. M., Deighan, J., et al.
 605 (2021). Enhanced water loss from the martian atmosphere during a regional-scale dust
 606 storm and implications for long-term water loss. *Earth and Planetary Science Letters*,
 607 571, 117109. <https://doi.org/10.1016/j.epsl.2021.117109>
- 608 Jakosky, B. M., Brain, D., Chaffin, M., Curry, S., Deighan, J., Grebowsky, J., et al. (2018).
 609 Loss of the Martian atmosphere to space: Present-day loss rates determined from
 610 MAVEN observations and integrated loss through time. *Icarus*, 315, 146–157.
 611 <https://doi.org/10.1016/j.icarus.2018.05.030>
- 612 Krasnopolsky, V. A. (2002). Mars' upper atmosphere and ionosphere at low, medium, and
 613 high solar activities: Implications for evolution of water: Mars' upper atmosphere and
 614 ionosphere. *Journal of Geophysical Research: Planets*, 107(E12), 11-1-11–11.
 615 <https://doi.org/10.1029/2001JE001809>
- 616 Krasnopolsky, V. A. (2019). Photochemistry of water in the martian thermosphere and its
 617 effect on hydrogen escape. *Icarus*, 321, 62–70.
 618 <https://doi.org/10.1016/j.icarus.2018.10.033>

- 619 Lefèvre, F., Lebonnois, S., Montmessin, F., & Forget, F. (2004). Three-dimensional
 620 modeling of ozone on Mars. *Journal of Geophysical Research E: Planets*, 109(7),
 621 E07004 1-20. <https://doi.org/10.1029/2004JE002268>
- 622 Lefèvre, F., Trokhimovskiy, A., Fedorova, A., Baggio, L., Lacombe, G., Määttänen, A., et al.
 623 (2021). Relationship Between the Ozone and Water Vapor Columns on Mars as
 624 Observed by SPICAM and Calculated by a Global Climate Model. *Journal of*
 625 *Geophysical Research: Planets*, 126(4). <https://doi.org/10.1029/2021JE006838>
- 626 Maltagliati, L., Montmessin, F., Fedorova, A., Korablev, O., Forget, F., & Bertaux, J.-L.
 627 (2011). Evidence of Water Vapor in Excess of Saturation in the Atmosphere of Mars.
 628 *Science*, 333(6051), 1868–1871. <https://doi.org/10.1126/science.1207957>
- 629 Maltagliati, L., Montmessin, F., Korablev, O., Fedorova, A., Forget, F., Määttänen, A., et al.
 630 (2013). Annual survey of water vapor vertical distribution and water-aerosol coupling in
 631 the martian atmosphere observed by SPICAM/MEx solar occultations. *Icarus*, 223,
 632 942–962. <https://doi.org/10.1016/j.icarus.2012.12.012>
- 633 McElroy, M. B., & Donahue, T. M. (1972). Stability of the Martian Atmosphere. *Science*,
 634 177(4053), 986–988. <https://doi.org/10.1126/science.177.4053.986>
- 635 Millour, E., Forget, F., Spiga, A., Vals, M., Zakharov, A. V., Navarro, T., et al. (2017). The
 636 Mars Climate Database (MCD version 5.3). In *proceedings from the 19th EGU General*
 637 *Assembly*, EGU2017, 23-28 April, 2017 in Vienna, Austria, p. 12247.
- 638 Montabone, L., Forget, F., Millour, E., Wilson, R. J., Lewis, S. R., Cantor, B., et al. (2015).
 639 Eight-year climatology of dust optical depth on Mars. *Icarus*, 251, 65–95.
 640 <https://doi.org/10.1016/j.icarus.2014.12.034>
- 641 Nair, H. (1994). A Photochemical Model of the Martian Atmosphere. *Icarus*, 111(1), 124–
 642 150. <https://doi.org/10.1006/icar.1994.1137>
- 643 Navarro, T., Madeleine, J.-B., Forget, F., Spiga, A., Millour, E., Montmessin, F., &
 644 Määttänen, A. (2014). Global climate modeling of the Martian water cycle with
 645 improved microphysics and radiatively active water ice clouds. *Journal of Geophysical*
 646 *Research: Planets*, 119(7), 1479–1495. <https://doi.org/10.1002/2013JE004550>
- 647 Neary, L., Daerden, F., Aoki, S., Whiteway, J., Clancy, R. T., Smith, M., et al. (2020).
 648 Explanation for the Increase in High-Altitude Water on Mars Observed by NOMAD
 649 During the 2018 Global Dust Storm. *Geophysical Research Letters*, 47(7).
 650 <https://doi.org/10.1029/2019GL084354>
- 651 Parkinson, T. D., & Hunten, D. M. (1972). Spectroscopy and Aeronomy of O₂ on Mars.
 652 *Journal of the Atmospheric Sciences*, 29(7), 1380–1390. [https://doi.org/10.1175/1520-0469\(1972\)029<1380:SAAOOO>2.0.CO;2](https://doi.org/10.1175/1520-0469(1972)029<1380:SAAOOO>2.0.CO;2)
- 654 Richardson, M. I., & Wilson, R. J. (2002). A topographically forced asymmetry in the
 655 martian circulation and climate. *Nature*, 416, 298–301.
- 656 Rodin, A., Korablev, O., & Moroz, V. (1997). Vertical Distribution of Water in the Near-
 657 Equatorial Troposphere of Mars: Water Vapor and Clouds. *Icarus*, 125(1), 212–229.
 658 <https://doi.org/10.1006/icar.1996.5602>
- 659 Scheller, E. L., Ehlmann, B. L., Hu, R., Adams, D. J., & Yung, Y. L. (2021). Long-term
 660 drying of Mars by sequestration of ocean-scale volumes of water in the crust. *Science*,
 661 372(6537), 56–62. <https://doi.org/10.1126/science.abc7717>

- 662 Shaposhnikov, D. S., Medvedev, A. S., Rodin, A. V., & Hartogh, P. (2019). Seasonal Water
 663 “Pump” in the Atmosphere of Mars: Vertical Transport to the Thermosphere.
 664 *Geophysical Research Letters*, 46(8), 4161–4169.
 665 <https://doi.org/10.1029/2019GL082839>
- 666 [Shaposhnikov, D.S., Medvedev, A.S., Rodin, A.V., Yiğit, E., Hartogh, P., \(2022\). Martian](#)
 667 [Dust Storms and Gravity Waves: Disentangling Water Transport to the Upper](#)
 668 [Atmosphere. JGR Planets 127. <https://doi.org/10.1029/2021JE007102>](#)
- 669 Stone, S. W., Yelle, R. V., Benna, M., Lo, D. Y., Elrod, M. K., & Mahaffy, P. R. (2020).
 670 Hydrogen escape from Mars is driven by seasonal and dust storm transport of water.
 671 *Science*, 370(6518), 824–831. <https://doi.org/10.1126/science.aba5229>
- 672 Vandaele, A. C., Korabiev, O., Daerden, F., Aoki, S., Thomas, I. R., Altieri, F., et al. (2019).
 673 Martian dust storm impact on atmospheric H₂O and D/H observed by ExoMars Trace
 674 Gas Orbiter. *Nature*, 568(7753), 521–525. <https://doi.org/10.1038/s41586-019-1097-3>